scientific reports

Check for updates

OPEN

Impacts of Mg doping on the structural properties and degradation mechanisms of a Li and Mn rich layered oxide cathode for lithium-ion batteries

Songyoot Kaewmala[1], Natthapong Kamma[2], Sunisa Buakeaw[3], Wanwisa Limphirat[4], Jeffrey Nash[1], Sutham Srilomsak[1,2], Pimpa Limthongkul[3] & Nonglak Meethong[1,2]✉

The Li- and Mn-rich layered oxide cathode material class is a promising cathode material type for high energy density lithium-ion batteries. However, this cathode material type suffers from layer to spinel structural transition during electrochemical cycling, resulting in energy density losses during repeated cycling. Thus, improving structural stability is an essential key for developing this cathode material family. Elemental doping is a useful strategy to improve the structural properties of cathode materials. This work examines the influences of Mg doping on the structural characteristics and degradation mechanisms of a $Li_{1.2}Mn_{0.4}Co_{0.4}O_2$ cathode material. The results reveal that the prepared cathode materials are a composite, exhibiting phase separation of the Li_2MnO_3 and $LiCoO_2$ components. Li_2MnO_3 and $LiCoO_2$ domain sizes decreased as Mg content increased, altering the electrochemical mechanisms of the cathode materials. Moreover, Mg doping can retard phase transition, resulting in reduced structural degradation. $Li_{1.2}Mn_{0.36}Mg_{0.04}Co_{0.4}O_2$ with optimal Mg doping demonstrated improved electrochemical performance. The current work provides deeper understanding about the roles of Mg doping on the structural characteristics and degradation mechanisms of Li-and Mn-rich layered oxide cathode materials, which is an insightful guideline for the future development of high energy density cathode materials for lithium-ion batteries.

Lithium-ion batteries have been used as energy storage devices for large-scale systems, electronic tools, and electric vehicles. This is because they exhibit higher energy density that those of other commercial battery technologies such Pd-acid, Ni–Cd, and Ni–MH batteries. The performance of lithium-ion batteries greatly depends on the electrochemical properties of their electrode materials, especially the cathode materials. Cathode materials contain Li ions in their structure. So, the electrochemical properties of cathode materials strongly affect the performance of lithium-ion batteries, including power and energy density. Currently, the utilization of Li-ion batteries has been exponentially increasing. There have been numerous efforts to explore new cathode materials with higher specific energy densities and lower costs to replace currently used commercial cathodes such as $LiCoO_2$, $LiFePO_4$ (LFP), and $LiNi_{1-x-y}Co_xMn_yO_2$ (NMC) materials. Li- and Mn-rich layered oxides, $xLi_2MnO_3{\cdot}(1-x)LiMO_2$ (M=Mn, Fe, Co, Ni, etc.), are promising cathode materials that can deliver high specific capacities of over 250 mAh/g[1–3]. However, use of this cathode material class has several problems, including low cycling stability, poor rate performance, and large voltage decay. These result from transition from a layered to a spinel-like structure during electrochemical cycling[4–7]. Previous studies reported that cation or anion substitution is an effective strategy to hinder structural transition during electrochemical cycling. Na^{+}[8–10], K^{+}[11], Al^{3+}[12,13], Ru^{4+}[14,15], Zn^{2+}[16,17], Mg^{2+}[18–21], F^{-}[22–24], and S^{2-}[25] doped Li and Mn rich layered oxide cathode materials present improved cycling stability. Wang and co-workers showed that $Li_{1.2}Ni_{0.2}Mn_{0.6}O_2$ doped by Mg in both Ni and Mn

[1]Institute of Nanomaterials Research and Innovation for Energy (IN-RIE), Khon Kaen University, Khon Kaen 40002, Thailand. [2]Materials Science and Nanotechnology Program, Department of Physics, Faculty of Science, Khon Kaen University, Khon Kaen 40002, Thailand. [3]National Energy Technology Center, National Science and Technology Development Agency, 111 Thailand Science Park, Phaholyothin Rd., Klong 1, Klong Luang 12120, Pathumthani, Thailand. [4]Synchrotron Light Research Institute, 111 University Avenue, Suranaree, Muang, Nakhon Ratchasima 30000, Thailand. ✉email: nonmee@kku.ac.th

sites exhibited higher cycling stability and conductivity compared to undoped material[18]. Nayak and co-workers reported that $Li_{1.2}Ni_{0.16}Mn_{0.56}Co_{0.08}O_2$ cathode materials with the proper amount of Mg doped into the Mn site revealed a retarded phase transition from a layered to a spinel structure during cycling, resulting in enhanced cycling stability[20]. Additionally, Jin and co-workers reported improved rate capability in $0.4Li_{4/3}Mn_{2/3}O_2{\cdot}0.6LiNi_{1/3}Co_{1/3}Mn_{1/3}O_2$ with the appropriate amount of Mg doping in Li sites. Such doping induced expanded lithium-ion diffusion channels, facilitating Li-ion transport[21]. This indicates that Mg substitution is helpful in improving the electrochemical performance of Li- and Mn-rich layered oxide cathode materials. Although Mg doping has been used to improve the electrochemical performance of cathode materials, deeper understanding of its impacts on the structural properties and degradation behaviors during prolonged cycling is not well developed. This is essentially important for developing cathode materials to meet practical applications.

The current work aims to investigate the impacts of Mg doping on the structural characteristics and degradation mechanisms during cycling of $Li_{1.2}Mn_{0.4}Co_{0.4}O_2$ cathode materials. X-ray absorption spectroscopy (XAS) and X-ray diffraction (XRD) techniques were used to study the local atomic structure and crystal structure of the prepared $Li_{1.2}Mn_{0.4}Co_{0.4}O_2$ and $Li_{1.2}Mn_{0.4-x}Mg_xCo_{0.4}O_2$ (x = 0.00, 0.02, 0.04, and 0.06) cathodes, respectively. Moreover, transmission electron microscopy (TEM) was employed to examine the microstructure and morphology of the materials. The electrochemical mechanisms, electrochemical performance, and lithium-ion diffusion coefficients of the electrodes were studied using galvanostatic cycling testing and a galvanostatic intermittent titration technique (GITT). The results imply that Mg doping not only play critical roles in development of the local atomic and crystal structure as reported the previous works, but also significantly impacts the phase separation behaviors of Li_2MnO_3- and $LiCoO_2$-like phases, altering the electrochemical mechanisms and properties of the prepared electrode materials. Furthermore, Mg doping has significant impacts on phase transformation and structural degradation mechanisms of cathode materials during cycling. Optimal Mg doping can retard spinel-like phase transition and consequently lead to improved electrochemical properties. The obtained results are an essential key to developing the electrochemical properties of Li- and Mn-rich layered oxide cathode materials.

Results and discussion

Morphological and microstructural characterization. Transmission electron microscopy (TEM) was employed to analyze the particle size distribution and morphology of the obtained cathode materials, as shown in Fig. S1. The prepared cathodes had broad particle size distributions of around 40 nm to 200 nm with average particle sizes of 118.00 ± 34.03 nm, 105.25 ± 28.31 nm, 107 ± 22.65 nm, and 105 ± 89 nm for $Li_{1.2}Mn_{0.4}Co_{0.4}O_2$, $Li_{1.2}Mn_{0.38}Mg_{0.02}Co_{0.4}O_2$, $Li_{1.2}Mn_{0.36}Mg_{0.04}Co_{0.4}O_2$, and $Li_{1.2}Mn_{0.34}Mg_{0.06}Co_{0.4}O_2$, respectively. Figure 1 presents images obtained from high resolution transmission electron microscopy (HRTEM) of the synthesized materials. At least five individual particles with sizes of approximately 100 nm, which is close to the average particle size of the materials, were chosen to study by HRTEM. Li_2MnO_3-like and $LiCoO_2$-like domains were clearly detected as monoclinic Li_2MnO_3 within space group $C2/m$ and rhombohedral $LiCoO_2$ within space group $R\bar{3}m$, respectively. Magnified images corresponding to the dashed green rectangles are demonstrated in Fig. S2. The $LiCoO_2$ regions show a continuous atomic structure along the Li and TM layers, whereas the Li_2MnO_3 regions show a periodic structure associated with the presence of Li in the transition metal layers. This makes the boundaries of the regions between these two phases easily observable, which are represented by red lines that show the interfaces between the $LiMO_2$ and the Li_2MnO_3 regions. The presence of both Li_2MnO_3-like and $LiCoO_2$-like regions in individual particles is consistent with previous work[1,26–31]. The experimental results reflect that the prepared samples are composite materials. Our previous reports illustrated that the domain size of the Li_2MnO_3 phase has significant influence on the electrochemical properties of composite-based Li- and Mn-rich layered oxide cathode materials. Varying Li_2MnO_3 domain sizes can alter Li_2MnO_3 activation, largely affecting the degree of transition from a layered to a spinel structure during electrochemical cycling[30,32,33]. From our experimental results, the domain sizes of Li_2MnO_3-like and $LiCoO_2$-like phases are strongly related to the Mg content. The domain sizes of both Li_2MnO_3-like and $LiCoO_2$-like phases decreased as the Mg content increased, as shown in Table S1. An undoped $Li_{1.2}Mn_{0.4}Co_{0.4}O_2$ electrode had the largest Li_2MnO_3- and $LiCoO_2$-like domain sizes, while $Li_{1.2}Mn_{0.34}Mg_{0.06}Co_{0.4}O_2$, with the highest level of Mg doping, revealed the smallest Li_2MnO_3- and $LiCoO_2$-like domain sizes. Mg doping and changes in the Li_2MnO_3-like domains significantly affected the electrochemical properties of the prepared materials, as seen in the electrochemical results. To confirm Mg doping, energy dispersive X-ray spectroscopy (EDS) was used to investigate elemental mapping, as shown in Fig. S3. The results reveal that the O, Mn, Co, and Mg (for Mg doped materials) species are uniformly distributed throughout the specimens. Clear particle surfaces, observed in the TEM images of Fig. S1, suggest that there were no surface coatings on the particles of the Mg-doped materials. This indicates that Mg was successfully doped into the bulk of the Mg-doped cathode materials.

Crystal and local atomic structure characterization. X-ray diffraction (XRD) was employed to examine the crystal structure of the synthesized cathode materials. The results are presented in Fig. 2. The X-ray diffraction patterns of the electrode materials correspond to those of both monoclinic Li_2MnO_3 within space group $C2/m$ and rhombohedral $LiCoO_2$ within space group $R\bar{3}m$ with the structural characteristics of layered α-$NaFeO_2$. Furthermore, the undoped material ($Li_{1.2}Mn_{0.4}Co_{0.4}O_2$) revealed diffraction peaks corresponding to Li_2MnO_3 and $LiCoO_2$ phases that are clearly separate at 2θ positions above 35°. For the Mg-doped materials ($Li_{1.2}Mn_{0.4-x}Mg_xCo_{0.4}O_2$ (x = 0.02, 0.04, and 0.06)), decreased XRD peak separation was observed that depended upon Mg content. The doped materials with higher Mn contents, including $Li_{1.2}Mn_{0.36}Mg_{0.04}Co_{0.4}O_2$ and $Li_{1.2}Mn_{0.34}Mg_{0.06}Co_{0.4}O_2$, showed well merged XRD peaks of the Li_2MnO_3 and $LiCoO_2$ phases, as presented in Fig. S4. This reflects that Mg doping has a significant effect on the crystal structure of as-prepared cathode materials. Mg doping can increase the degree of mixing between Li_2MnO_3 and $LiCoO_2$ phases. This was

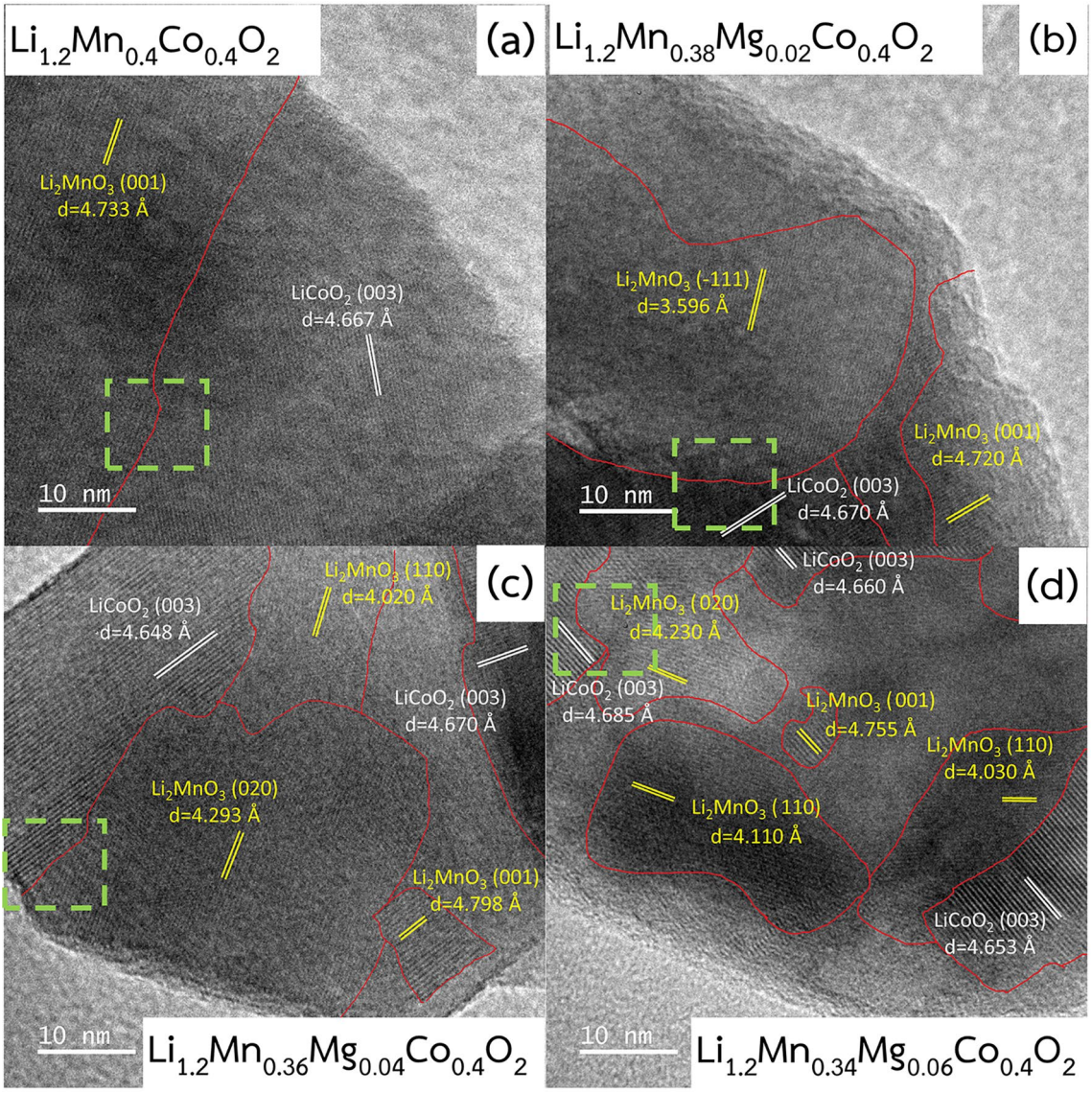

Figure 1. HRTEM images of the pristine $Li_{1.2}Mn_{0.4}Co_{0.4}O_2$ and Mg-doped $Li_{1.2}Mn_{0.4}Co_{0.4}O_2$materials.

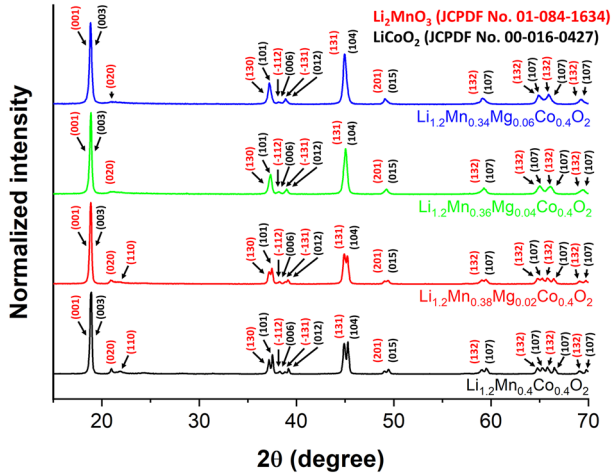

Figure 2. X-ray diffraction spectra of the pristine $Li_{1.2}Mn_{0.4}Co_{0.4}O_2$ and Mg-doped $Li_{1.2}Mn_{0.4}Co_{0.4}O_2$ materials.

especially observed in $Li_{1.2}Mn_{0.36}Mg_{0.04}Co_{0.4}O_2$ and $Li_{1.2}Mn_{0.34}Mg_{0.06}Co_{0.4}O_2$ materials. Doping with Mg^{2+} can significantly reduce the mixing energy between the Li_2MnO_3 and $LiCoO_2$ phases, leading to a higher degree of mixing between these phases compared with an undoped cathode material. This phenomenon was confirmed by high-resolution transmission electron microscopy (HRTEM) in Fig. 1. Moreover, Rietveld refinement was performed to study the influences of Mg doping on the structural properties of $Li_{1.2}Mn_{0.4}Co_{0.4}O_2$ electrodes, as demonstrated in Fig. S5. Information about related atomic positions is given in Table S2. The calculated lattice constants are presented in Table S3. These results illustrate that the unit cell volume decreased as Mg content increased, as shown in Fig. S6a. Additionally, β was also reduced when the level of Mg doping increased, as presented in Fig. S6b. This indicates that Mg doping significantly induced structural distortion in $Li_{1.2}Mn_{0.4}Co_{0.4}O_2$ materials. XRD results show more broad and merged peaks when the Mg content is increased. This may introduce inaccuracies into XRD analysis of the Mg position. Thus, X-ray absorption spectroscopy, which is sensitive to the local atomic structure of materials, was used to investigate the Mg position in Mg-doped materials.

An XAS technique was employed to study the local atomic structure of pristine $Li_{1.2}Mn_{0.4}Co_{0.4}O_2$ and Mg-doped $Li_{1.2}Mn_{0.4}Co_{0.4}O_2$ materials. Figure 3 illustrates the XANES spectra at Mn and Co *K*-edges of the prepared cathodes compared with the XANES spectra of Li_2MnO_3 and $LiCoO_2$ phases as references. It is found that the XANES features of the obtained cathodes are almost identical to those of Li_2MnO_3 and $LiCoO_2$ phases at the Mn and Co *K*-edges, respectively. This can be ascribed to the composite behavior of the synthesized cathode materials. The synthesized cathodes consist of Li_2MnO_3– and $LiCoO_2$-like regions, corresponding to the HRTEM and XRD results. The oxidation states of the Mn and Co species are directly determined by the main absorption edge positions. At Mn and Co *K*-edges, undoped $Li_{1.2}Mn_{0.4}Co_{0.4}O_2$ and Mg-doped $Li_{1.2}Mn_{0.4}Co_{0.4}O_2$ materials showed primary absorption edges at the same position, confirmed by 1st derivatives of XAS spectra, as illustrated in Fig. S7. This indicates that Mn and Co atoms in these materials have the same valance states. Moreover, the XANES profiles are identical to those in previous reports using XAS techniques to examine the same cathode material type. Mn and Co atoms possess average valance states of 4 + and 3 +, respectively[34–36]. The XANES spectra at both the Mn and Co edges of pristine undoped $Li_{1.2}Mn_{0.4}Co_{0.4}O_2$ and Mg-doped $Li_{1.2}Mn_{0.4}Co_{0.4}O_2$ materials largely overlapped with small differences between them. This suggests that Mn and Co atoms in the materials are in similar environments with similar local atomic structures and slightly different structural distortion. Additionally, Figs. 3c and 4d reveal k^2-weighted Fourier-transformed EXAFS signals at the Mn and Co *K*-edges of pristine $Li_{1.2}Mn_{0.4}Co_{0.4}O_2$ and Mg-doped $Li_{1.2}Mn_{0.4}Co_{0.4}O_2$, materials, respectively. The first main

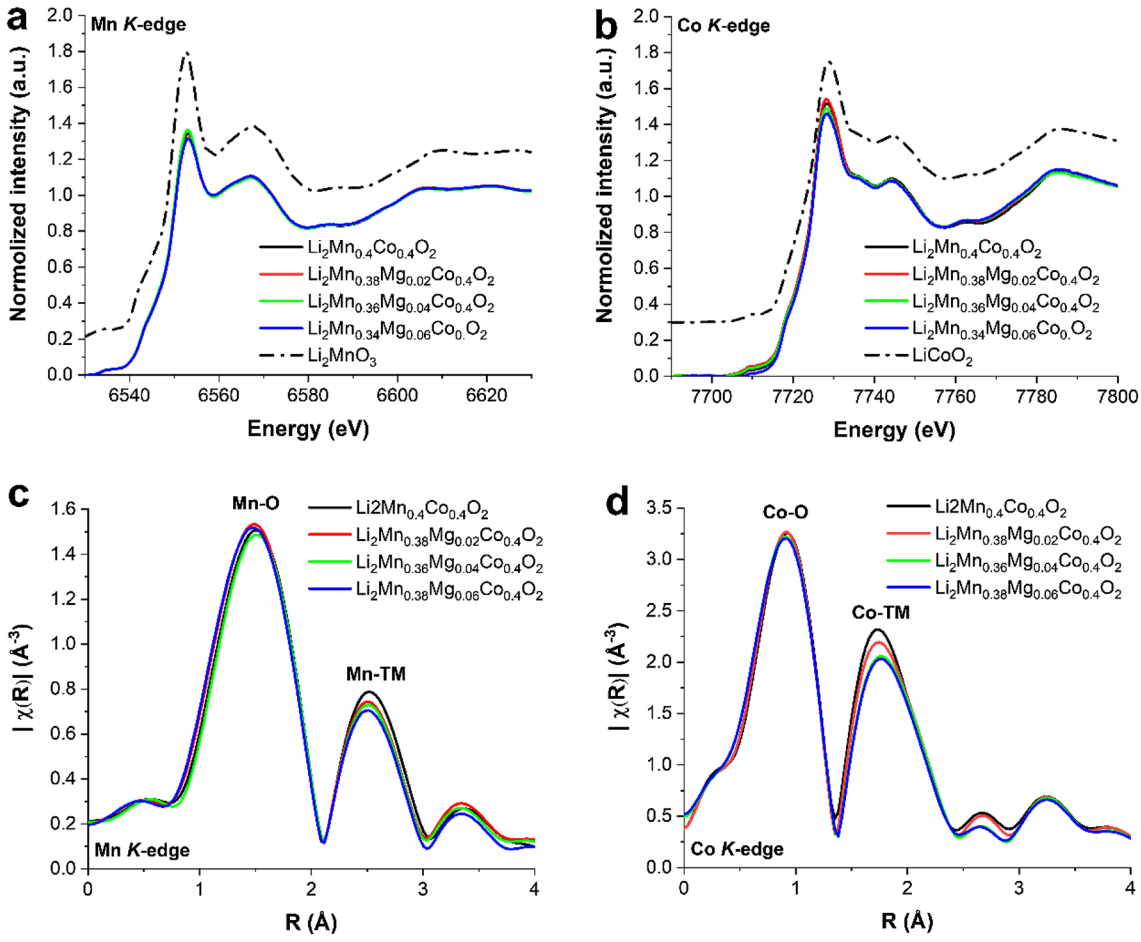

Figure 3. XANES profiles and k^2-weighted Fourier-transformed EXAFS signals at the Mn (**a** and **c**) and Co (**b** and **d**) *K*-edges of pristine $Li_{1.2}Mn_{0.4}Co_{0.4}O_2$, Mg-doped $Li_{1.2}Mn_{0.4}Co_{0.4}O_2$, Li_2MnO_3, and $LiCoO_2$ materials.

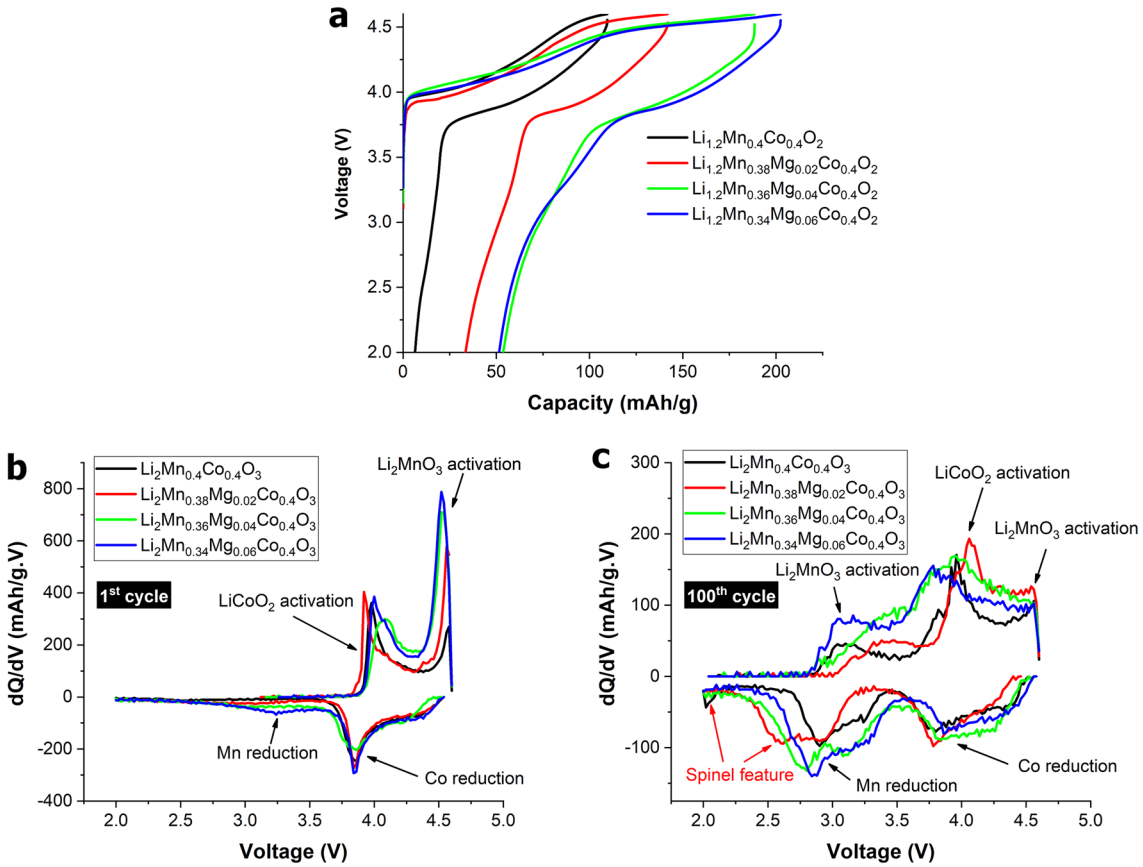

Figure 4. Voltage profiles (**a**), differential capacity plots at the 1st cycle (**b**), and differential capacity plots at the 100th cycle (**c**) of pristine $Li_{1.2}Mn_{0.4}Co_{0.4}O_2$ and Mg-doped $Li_{1.2}Mn_{0.4}Co_{0.4}O_2$ materials cycled at C/3.

peaks occurred because the interactions between Mn and Co adsorbing atoms, located in the octahedral sites, were surrounded by six oxygen atoms. The peaks are denoted as Mn–O and Co–O for the Mn and Co *K*-edges, respectively. The second peaks correspond to the interactions between Mn and Co adsorbing atoms and transition metal (TM) atoms in the transition metal layers. The peaks are denoted as Mn-TM and Co-TM for the Mn and Co *K*-edges, respectively. It is well established that the amplitudes of the Mn-TM and Co-TM peaks are highly sensitive to surrounding elements. Our previous work studying the same material type reported that $Li_{1.2}Mn_{0.4}Co_{0.4}O_2$ materials with various Li_2MnO_3 and $LiCoO_2$ domain sizes provided different intensities of the Mn-TM and Co-TM peaks. This is occurred because Mn and Co are surrounded by different types and numbers of neighboring atoms that have different X-ray scattering capabilities[32]. In the current study, at the Co-*K* edge, the amplitude of Co-TM peak is decreased with the Li_2MnO_3 and $LiCoO_2$ domain size (Mn content increased). This is because the Li_2MnO_3 and $LiCoO_2$ phases are more distributed in the material with smaller Li_2MnO_3 and $LiCoO_2$ domain sizes, while the individual Li_2MnO_3 and $LiCoO_2$ phases are more locally isolated in the material with larger Li_2MnO_3 and $LiCoO_2$ domain sizes. The result is that Co atoms in the material with smaller Li_2MnO_3 and $LiCoO_2$ domain sizes interact with a larger number of Mn atoms (lighter atoms). There is less scattering than Co and consequently a lower amplitude Co-TM peak is produced. At the Mn-*K* edge, our previous report[32] presented that a $Li_{1.2}Mn_{0.4}Co_{0.4}O_2$, material with a smaller Li_2MnO_3 domain size exhibited a stronger intensity of the Mn-TM peak. This is occurred because the Mn atoms are surrounded by a larger Co species, leading to better scattering than for Mn alone and increased amplitude of the Mn-TM peak. In contrast, the current study showed that Mg-doped cathode materials reveal decreased amplitude of Mn-TM although Li_2MnO_3 and $LiCoO_2$ domain sizes decreased (Mn content increased). This results from the presence of Mg in transition metal layers, which has a very low x-ray scattering power compared with Mn and Co species. So, the intensity of the Mn-TM peak decreased as the Mg content increased. The XAS experimental results revealed that the domain sizes of Li_2MnO_3 and $LiCoO_2$ phases decreased when the Mg content increased, which is in complete agreement with the XRD and HRTEM results. Additionally, the decreased amplitude of Mn-TM is evidence of the presence of Mg in Mn-sites in the transition metal layers of the Li_2MnO_3 structure. Moreover, EXAFS fitting was performed to calculate the chemical bond lengths of Mn–O, Mn-TM, Co–O, and Co-TM to obtain deeper information involving the impacts of Mg doping on the local structure of Mg-doped $Li_{1.2}Mn_{0.4}Co_{0.4}O_2$ materials. Fourier-transformed EXAFS signals with fitted spectra at the Mn and Co *K*-edges are given in Figs. S8 and S9, respectively. The calculated bond distances and agreement indices are presented in Table S4. These results imply that Mg doping significantly decreases the Mn–O bond length with increasing Mg content, as can be seen in

Fig. S10. This suggests that Mg doping can probably strengthen the chemical bonds and reinforce interactions of MnO_6-octahedral slabs, leading to improved structural stability[37].

Electrochemical characterization. The electrochemical performance of the prepared electrodes was examined using galvanostatic cycling, as illustrated in Fig. S11. Figure 4a shows the voltage profiles obtained during the initial cycle. The voltage profiles of the electrode consist of two notable plateaus at around 3.9 V and 4.4 V, corresponding to activation of the $LiCoO_2$ and Li_2MnO_3 components, respectively. For composite-based Li- and Mn-rich layered oxide cathodes, it is established that the Li_2MnO_3 phase has an important role in storing excess lithium for stabilizing the $LiMO_2$ component (M=Co, Ni, and Mn), bringing about improved structural stability during electrochemical cycling[18,31,38,39]. The electrochemical mechanism of the prepared cathode materials can be explained as follows. During the initial charging process at around 3.9 V to 4.4 V, Li ions are extracted from the $LiCoO_2$ structure to form a CoO_2 phase, resulting in the oxidation of Co^{3+} to Co^{4+}, while the Li_2MnO_3 component is electrochemically inactive. This causes depletion of Li ions in the lithium layers of the $LiCoO_2$ structure. Li ions from octahedral sites in the Li and Mn layers of the Li_2MnO_3 component subsequently diffuse into the lithium-depleted layers of the $LiCoO_2$ structure to maintain structural stability[40,41]. For the second voltage plateau, at about 4.4 V to 4.6, Li ions are extracted from the Li_2MnO_3 structure to produce Li_2O and layered MnO_2 phases. Formation of a Li_2O phase results in irreversible capacity loss in the initial cycle[31,38]. During the discharge process, a Li ion is inserted into the $Li_{1-x}CoO_2$ structure at around 4.6–3.8 V, while a Li ion is inserted into MnO_2 phases below 3.8 V, corresponding to a reduction of Mn^{4+} to Mn^{3+} to form a layered $LiMnO_2$ phase. It is established that the formed $LiMnO_2$ phase always experiences transition from a layered to a spinel-like structure upon electrochemical cycling, which subsequently induces a large capacity loss and voltage drop during repeated cycling. This indicates that the activation of Li_2MnO_3 to form a $LiMnO_2$ phase can induce a spinel-like phase transition during cycling. Previous reports revealed that the degree of Li_2MnO_3 activation is largely determined by the Li_2MnO_3 domain size and current rate[33,42,43]. A small Li_2MnO_3 domain size and low current rate could facilitate activation of the Li_2MnO_3 phase and subsequently cause a large initial irreversible capacity and a spinel-like phase transition, leading to poor cyclability. This is shown in the electrochemical results observed in the initial voltage profiles of the prepared electrodes, given in Fig. 4a. The initial irreversible capacities of $Li_{1.2}Mn_{0.4}Co_{0.4}O_2$, $Li_{1.2}Mn_{0.38}Mg_{0.02}Co_{0.4}O_2$, $Li_{1.2}Mn_{0.36}Mg_{0.04}Co_{0.4}O_2$, and $Li_{1.2}Mn_{0.34}Mg_{0.06}Co_{0.4}O_2$ cathodes are 6.39 mAh/g, 33.46 mAh/g, 53.67 mAh/g, and 51.47 mAh/g, respectively. This indicates that an electrode with a smaller Li_2MnO_3 domain size can allow a larger level of Li_2MnO_3 activation, which is directly related to the range of the voltage plateau at around 4.4 V. A larger activation brings about higher initial irreversible capacity. This is because a smaller Li_2MnO_3 domain size is easier to activate. Figure 4b shows differential capacity plots at the 1st cycle of the electrode materials. The oxidation peaks at around 3.9 V and 4.5 V result from $LiCoO_2$ and Li_2MnO_3 activation, respectively. The degree of Li_2MnO_3 activation is directly correlated with the intensity of the oxidation peak at 4.5 V. Mg-doped cathodes reveal a higher oxidation peak intensity at 4.5 V than undoped cathodes. This is because the cathodes with smaller Li_2MnO_3 domain sizes induce greater Li_2MnO_3 activation, especially for $Li_{1.2}Mn_{0.36}Mg_{0.04}Co_{0.4}O_2$, and $Li_{1.2}Mn_{0.34}Mg_{0.06}Co_{0.4}O_2$ cathodes. Figure 4c presents differential capacity plots after the 100th cycle for the electrode materials. The results show that the oxidation peak at 4.5 V almost disappears because most of the Li_2MnO_3 component has been activated to form a $LiMnO_2$ phase. The reduction peaks at about 3.9 V and 2.8 V correspond to Li-ion insertion into the CoO_2 and MnO_2 phases to form $LiCoO_2$ and $LiMnO_2$, respectively. An undoped cathode ($Li_{1.2}Mn_{0.4}Co_{0.4}O_2$) shows a small oxidation peak at 2.0 V, corresponding to spinel-like phase features[33]. Furthermore, a Mg-doped cathode with a low Mn content ($Li_{1.2}Mn_{0.38}Mg_{0.02}Co_{0.4}O_2$) reveals a shift of the reduction peak at 2.8 V to a lower voltage of around 2.5 V, indicating that the cathode exhibits a spinel-like phase evolution during electrochemical cycling[44–46]. In contrast, the $Li_{1.2}Mn_{0.36}Mg_{0.04}Co_{0.4}O_2$ and $Li_{1.2}Mn_{0.34}Mg_{0.06}Co_{0.4}O_2$ cathodes reveal a smaller degree of peak shift toward lower voltages. This indicates that doping a $Li_{1.2}Mn_{0.4}Co_{0.4}O_2$ cathode with an appropriate Mg content can help to suppress spinel-like phase transition during cycling. According to XAS experimental results, for Mg-doped cathodes, Mg doping decreases the bond length between Mn and O (Mn–O), suggesting that Mg substitution strengthens the chemical bonds and reinforces interactions of the MnO_6-octahedral slabs, leading to enhanced structural stability. Additionally, this suggests that the level of structural transition highly depends on Mg content. Figure 5a shows that the $Li_{1.2}Mn_{0.36}Mg_{0.04}Co_{0.4}O_2$ and $Li_{1.2}Mn_{0.34}Mg_{0.06}Co_{0.4}O_2$ cathodes have higher reversible capacity than other cathodes. This phenomenon results from a smaller Li_2MnO_3 domain size that causes a larger level of Li_2MnO_3 to form a greater amount of the electrochemically active MnO_2 phase, leading to higher reversible capacity. Additionally, the $Li_{1.2}Mn_{0.36}Mg_{0.04}Co_{0.4}O_2$ cathode has higher cycling stability than other candidate cathodes. This indicates that $Li_{1.2}Mn_{0.36}Mg_{0.04}Co_{0.4}O_2$ is an optimal Mn doping (x = 0.04) condition, while cathodes with higher Mg doping ($Li_{1.2}Mn_{0.34}Mg_{0.06}Co_{0.4}O_2$, x = 0.06) show lower cycling stability than the $Li_{1.2}Mn_{0.36}Mg_{0.04}Co_{0.4}O_2$ cathode. Doping with a very high Mg content (x = 0.06) can induce a larger structural distortion, corresponding to severe decrease in the β value observed in Rietveld refinement results, as shown in Fig. S6b. Greater structural distortion can lead to poorer structural stability, producing cathodes with lower cyclability than the $Li_{1.2}Mn_{0.36}Mg_{0.04}Co_{0.4}O_2$ cathode. Moreover, the $Li_{1.2}Mn_{0.36}Mg_{0.04}Co_{0.4}O_2$ cathode also has noticeably better rate capability than other candidate cathodes, as revealed in Fig. 5b, since Li_2MnO_3 is electrochemically inert. Therefore, $Li_{1.2}Mn_{0.4}Co_{0.4}O_2$ and $Li_{1.2}Mn_{0.38}Mg_{0.02}Co_{0.4}O_2$ cathodes with a larger Li_2MnO_3 domain size often exhibit lower reversible capacity and poorer rate performance. Additionally, $Li_{1.2}Mn_{0.4}Co_{0.4}O_2$ and $Li_{1.2}Mn_{0.38}Mg_{0.02}Co_{0.4}O_2$ cathodes also exhibit a large structural transition during cycling. This structural transition can lead to severe structural disorder and larger defects. For $Li_{1.2}Mn_{0.34}Mg_{0.06}Co_{0.4}O_2$ at higher Mg doping, the cathode consists of the smallest Li_2MnO_3 domain size but has poor structural stability. This leads to structural degradation and defect formation during cycling, which hinders Li-ion transport in the electrode. These phenomena act as barriers for Li-ion mobility in cathode materials that consequently result in poorer rate

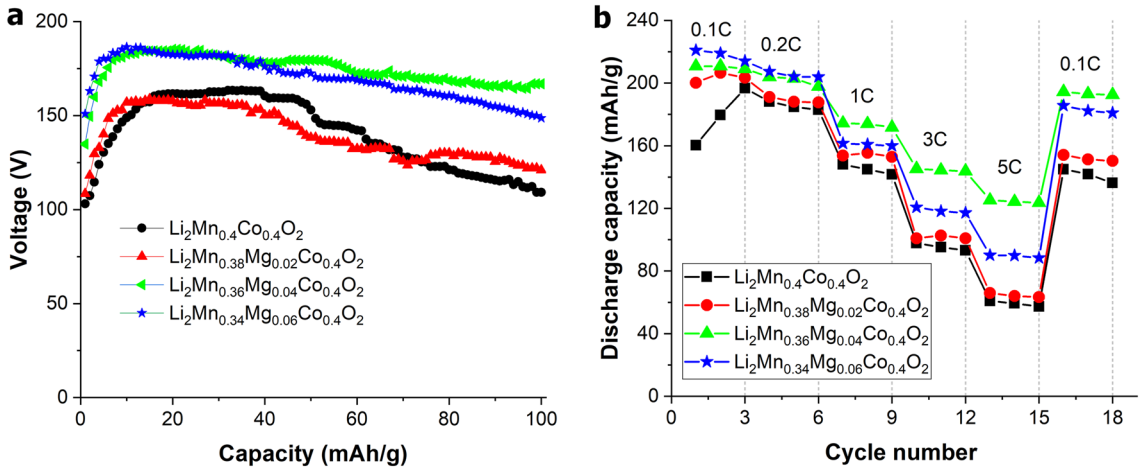

Figure 5. Cycling stability (**a**) and rate performance (**b**) of pristine $Li_{1.2}Mn_{0.4}Co_{0.4}O_2$ and Mg-doped $Li_{1.2}Mn_{0.4}Co_{0.4}O_2$ materials.

performance. This gives the $Li_{1.2}Mn_{0.36}Mg_{0.04}Co_{0.4}O_2$ cathode a smaller Li_2MnO_3 domain size and higher structural stability during electrochemical cycling, presenting higher rate capability than the other cathode materials. Interestingly, this is contrary to our previous works reporting that an undoped $Li_{1.2}Mn_{0.36}Mg_{0.04}Co_{0.4}O_2$ cathode with a smaller Li_2MnO_3 domain size had lower cycling stability that of the cathode with a larger Li_2MnO_3 domain size. This is because a small Li_2MnO_3 domain was easily activated and further transformed to a spinel-like phase, subsequently leading to more severe structural deterioration upon cycling[30,32]. It can be confirmed that Mg doping enhances structural stability of a cathode material.

Electrochemical impedance spectroscopy (EIS) was done to examine the electronic conductivity of the cathodes after 100 cycles, as shown in Fig. S12. The calculated charge transfer resistance (R_{CT}) is shown in Table S5. For fresh cells, $Li_{1.2}Mn_{0.4}Co_{0.4}O_2$, $Li_{1.2}Mn_{0.38}Mg_{0.02}Co_{0.4}O_2$, $Li_{1.2}Mn_{0.36}Mg_{0.04}Co_{0.4}O_2$, and $Li_{1.2}Mn_{0.34}Mg_{0.06}Co_{0.4}O_2$ cathodes revealed R_{CT} values of 9.235 Ω, 8.452 Ω, 8.324 Ω, and 8.624 Ω, respectively. After 100 cycles, the R_{CT} values were respectively 739.485Ω, 345.214 Ω, 305.236 Ω, and 479.258 Ω for these cathodes. $Li_{1.2}Mn_{0.36}Mg_{0.04}Co_{0.4}O_2$ exhibited the lowest R_{CT} among the cathodes after repeated cycling. This indicates that the other cathodes had a higher level of structural transition and degradation during electrochemical cycling, generating a greater degree of structural disorder and defects. These phenomena have negative impacts on both the ionic and electronic conductivities of the cathode materials.

The electrochemical cycling process of a Li-ion battery can be explained as Li-ion insertion and extraction in the structures of its electrode and cathode materials. This indicates that understanding the kinetic parameters impacting Li-ion diffusion coefficients of electrode materials is important to enable design and develop electrode materials for Li-ion batteries with good electrochemical performance. A galvanostatic intermittent titration technique (GITT) is widely used to investigate the lithium-ion mobility behaviors of electrode materials. The lithium-ion diffusion coefficient (D_{Li^+}) can be expressed by Fick's Second Law of Diffusion, as demonstrated in Eq. 1[47,48]:

$$D_{Li^+} = \frac{4}{\pi}\left(\frac{m_B V_M}{M_B S}\right)^2 \left(\frac{\Delta E_S}{\tau\left(\frac{dE_\tau}{d\sqrt{\tau}}\right)}\right)^2 \left(\tau << \frac{L^2}{D_{Li^+}}\right) \quad (1)$$

where m_B and M_B are the molecular weight and mass of the active material, respectively. V_m is the molar volume of the active material. S is defined as the surface area of the electrode. L is electrode thickness. Figure S13 reveals that the relationship between the cell voltage profile (E) and $t^{1/2}$ is nearly linear. Consequently, Eq. (1) can be simplified as[49,50]:

$$D_{Li^+} = \frac{4}{\pi\tau}\left(\frac{m_B V_M}{M_B S}\right)^2 \left(\frac{\Delta E_S}{\Delta E_\tau}\right)^2 \left(\tau << \frac{L^2}{D_{Li^+}}\right) \quad (2)$$

The electrochemical mechanisms of the Li and Mn rich layered oxide cathode material class are complex, involving lithium-ion diffusion, oxygen loss, and structural transformation. Therefore, this work emphasizes an investigation of the overall Li-ion diffusion coefficients of the prepared cathode materials. The calculated coefficients are defined as apparent Li-ion diffusion coefficients[51,52]. The GITT profiles and calculated lithium-ion diffusion coefficients as a function of time for $Li_{1.2}Mn_{0.4}Co_{0.4}O_2$ and $Li_{1.2}Mn_{0.36}Mg_{0.04}Co_{0.4}O_2$ cathode materials at the first and 100th cycles are revealed in Fig. S14. Figure 6a and b illustrate calculated lithium-ion diffusion coefficients as a function of cell voltage for $Li_{1.2}Mn_{0.4}Co_{0.4}O_2$ and Mg-doped $Li_{1.2}Mn_{0.4}Co_{0.4}O_2$ electrodes. In Fig. 6a and 6b, the charging process exhibits two distinct lithium-ion diffusion regions. The calculated lithium-ion diffusion coefficient values of the prepared cathode are very similar. The first region corresponds to the extraction of Li ions from the $LiCoO_2$ structure at voltages below 4.4 V. The calculated lithium-ion diffusion coefficients of the $Li_{1.2}Mn_{0.36}Mg_{0.04}Co_{0.4}O_2$ electrode are slightly higher than those of the other electrodes. These calculated

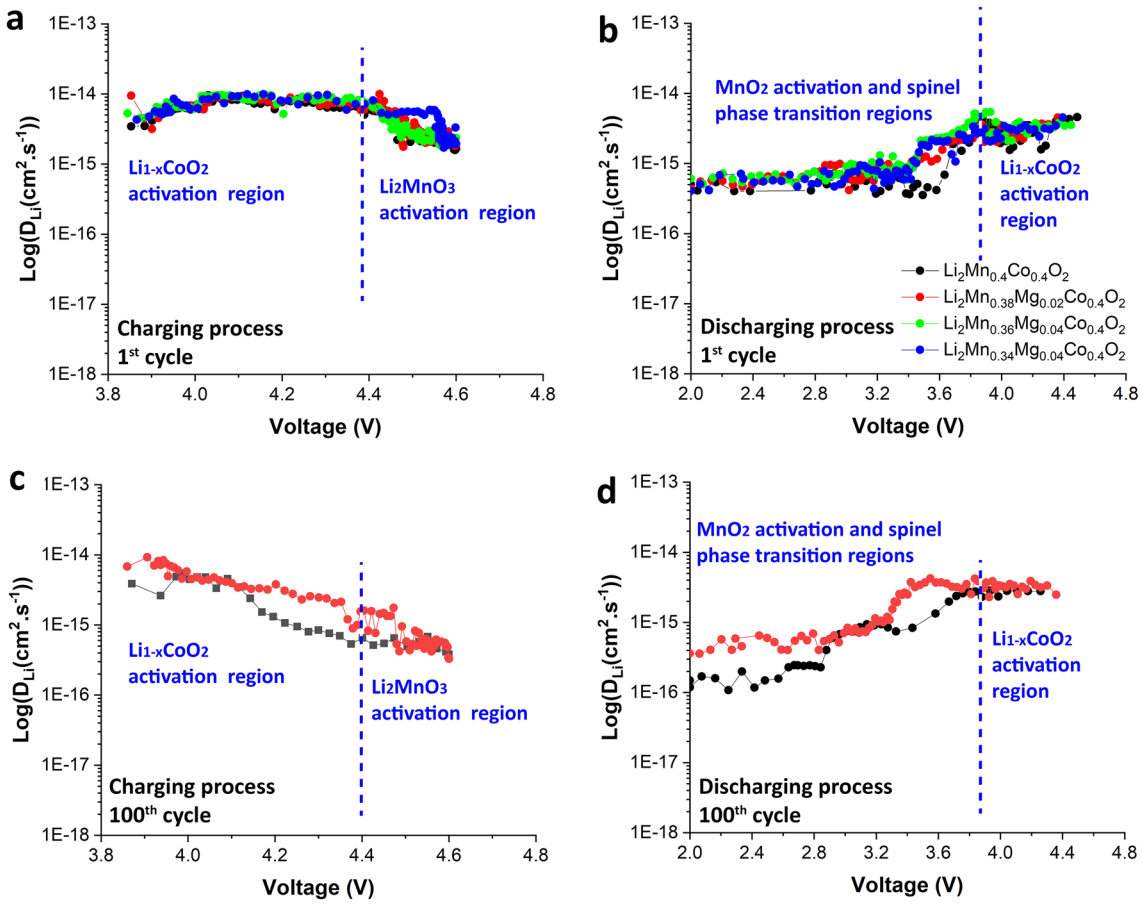

Figure 6. Calculated lithium-ion diffusion coefficients as a function of cell voltage at the 1st and 100th cycles during charging (**a** and **c**) and discharging (**b** and **d**) processes.

lithium-ion diffusion coefficients increased slightly from around 3.44×10^{-15} cm^2 s^{-1} to 9.57×10^{-15} cm^2 s^{-1} when the electrodes were charged to 4.04 V. Then, the coefficients decreased gradually from around 9.57×10^{-15} to 5.98×10^{-15} cm^2 s^{-1} when the electrodes were charged to 4.40 V. The second region is ascribed to extraction of Li ions from the Li_2MnO_3 component at voltages above 4.4 V. The calculated lithium-ion diffusion coefficients decreased rapidly from around 5.98×10^{-15} cm^2 s^{-1} to 1.66×10^{-18} cm^2 s^{-1} when the electrodes were charged to 4.6 V. This reveals that the Li-ion diffusion coefficients of the Li_2MnO_3 component are lower than those of the $LiCoO_2$ component due to the lower ionic conductivity of the Li_2MnO_3 component. For the initial discharge processes, the calculated lithium-ion diffusion coefficients of the $Li_{1.2}Mn_{0.36}Mg_{0.04}Co_{0.4}O_2$ electrode are slightly higher than those of the candidate electrodes. Two lithium-ion diffusion regions were clearly observed. The first region corresponds to Li-ion intercalation into the $Li_{1-x}CoO_2$ structure at higher voltages. The second region occurred from Li-ion intercalation into MnO_2 and a newly formed spinel phase at lower voltages. The Li-ion diffusion coefficients obtained from the $Li_{1-x}CoO_2$ activation region were higher than those of the MnO_2 and spinel structures. This occurred because of structural disorder and defects produced during the spinel phase transformation. The results show that the lithium-ion diffusion coefficient slightly increased with the Mg content, but the $Li_{1.2}Mn_{0.34}Mg_{0.06}Co_{0.4}O_2$ electrode with the highest Mg content shows lower a lithium-ion diffusion coefficient than $Li_{1.2}Mn_{0.36}Mg_{0.04}Co_{0.4}O_2$ electrode because a higher level of Mg doping induces a larger structural distortion, obstructing lithium-ion transport in the structure. This causes the Mg-doped cathodes to exhibit slightly improved rate capability, especially for the $Li_{1.2}Mn_{0.34}Mg_{0.06}Co_{0.4}O_2$ electrode, as demonstrated in Fig. 5b. Moreover, the calculated lithium-ion diffusion coefficients during charging and discharging processes of the prepared electrodes after 100 cycles are shown in Fig. 6c and d. The experimental results reveal that the $Li_{1.2}Mn_{0.04}Co0_{.4}O_2$ electrode exhibited lower Li-ion diffusion coefficients than those of the $Li_{1.2}Mn_{0.36}Mg_{0.04}Co_{0.4}O_2$ electrode. The reason for this is that the $Li_{1.2}Mn_{0.04}Co0_{.4}O_2$ electrode encounters a greater level of the spinel phase transition that subsequently results in more structural disorder and larger defects. This leads to severe structural degradation that hinders Li-ion diffusion, inducing slower Li-ion transport in the $Li_{1.2}Mn_{0.04}Co0_{.4}O_2$ cathode. These results imply that appropriate Mg doping ($x = 0.04$) can effectively help to stabilize the structure of Li- and Mn-rich layered oxide cathode materials. This gives the $Li_{1.2}Mn_{0.36}Mg_{0.04}Co_{0.4}O_2$ cathode material a higher cycling stability and noticeably better rate capability than other candidate cathodes.

XAS and HRTEM techniques were employed to examine the structural evolution of the $Li_{1.2}Mn_{0.4}Co_{0.4}O_2$ and $Li_{1.2}Mn_{0.36}Mg_{0.04}Co_{0.4}O_2$ cathodes after prolonged cycling. Figure 7a and b illustrate calculated and measured XANES spectra of a pristine electrode and cycled electrodes after 50 cycles for Mn and Co *K*-edges,

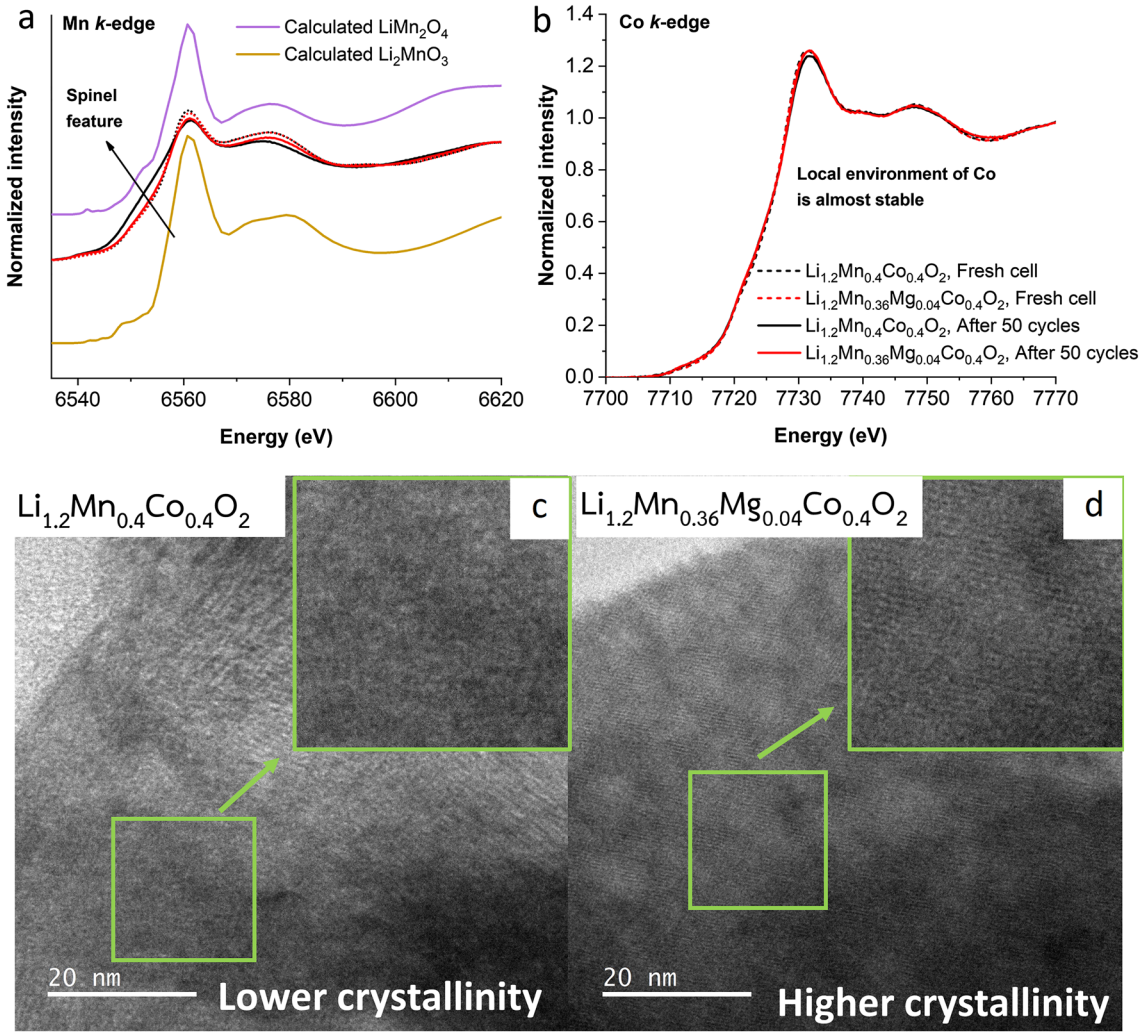

Figure 7. XANES spectra at Mn (**a**) and Co (**b**) *K*-edges of a fresh cell and cells cycled at various current rates after 50 cycles, HRTEM images of cycled $Li_{1.2}Mn_{0.4}Co_{0.4}O_2$ (**c**) and $Li_{1.2}Mn_{0.36}Mg_{0.04}Co_{0.4}O_2$ (**d**) electrodes after 100 cycles.

respectively. For the Mn *K*-edge, experimental results show that the local environment around the Mn atoms in the $Li_{1.2}Mn_{0.4}Co_{0.4}O_2$ cathode changed significantly, while that of $Li_{1.2}Mn_{0.36}Mg_{0.04}Co_{0.4}O_2$ cathodes slightly changed compared to the fresh cathodes. Especially in the case of $Li_{1.2}Mn_{0.4}Co_{0.4}O_2$ cathode, the rising-edge feature of the electrode was closer to the rising edge of a spinel $LiMn_2O_4$ phase than that of a $Li_{1.2}Mn_{0.4}Co_{0.4}O_2$ cathode. This indicates that proper Mg doping can retard structural transitions during electrochemical cycling. Additionally, for the Co *K*-edge, the local environment around the Co atoms was quite stable. However, a $Li_{1.2}Mn_{0.4}Co_{0.4}O_2$ cathode with a larger spinel phase evolution exhibited slight local environmental changes. HRTEM images of the $Li_{1.2}Mn_{0.4}Co_{0.4}O_2$ and $Li_{1.2}Mn_{0.36}Mg_{0.04}Co_{0.4}O_2$ cathodes were used to present the degree of overall structural degradation after 100 cycles, as seen in Fig. 7c and d. The $Li_{1.2}Mn_{0.4}Co_{0.4}O_2$ cathode exhibits lower crystallinity than the $Li_{1.2}Mn_{0.36}Mg_{0.04}Co_{0.4}O_2$ cathode. This results from a lager phase transition leading to more severe structural deterioration. It reflects that Mg doping can improve the overall structural stability of the Li- and Mn-layered oxide cathode material class upon cycling.

This work found that the prepared cathodes were of a composite material type consisting of Li_2MnO_3 and $LiCoO_2$ components, which was confirmed from HRTEM, XRD, and XAS results. Li_2MnO_3 and $LiCoO_2$ domain sizes decreased as the Mg content increased. The XRD results show more broad and merged peaks when the Mg content is increased. This may introduce inaccuracies into XRD analysis of the Mg position. Thus, X-ray absorption spectroscopy, which is sensitive to the local atomic structure of materials, was used to investigate the Mg position in Mg-doped materials. Various Li_2MnO_3 sizes play a critical role in the electrochemical behaviors of the prepared materials. This is because Li_2MnO_3, with a smaller domain size, can be easily activated, leading to higher reversible capacity. However, activation of the Li_2MnO_3 component always results in transition from a layered to a spinel-like structure upon electrochemical cycling. This brings about structural degradation and consequently poor electrochemical performance. Additionally, EDS and XAS results imply that Mg was successfully doped into Mn sites in the structure of the Li_2MnO_3 component. The electrochemical results reveal that appropriate Mg doping can improve the structural stability of a cathode material, leading to enhanced electrochemical

properties. The impacts of Mg doping on the microstructure and structural degradation mechanisms during repeated cycling of a composite-based Li-and Mn-rich layered oxide cathode material are displayed in Fig. 8. $Li_{1.2}Mn_{0.36}Mg_{0.04}Co_{0.4}O_2$ with small Li_2MnO_3 domain sizes exhibited improved electrochemical performance. In this study, the electrochemical performance of the synthesized cathode materials is lower than those of Li-and Mn-rich layered oxide cathode materials in previous work. The obtained information reveals deeper understanding about the roles of Mg doping on the structural characteristics, electrochemical properties, and structural degradation mechanisms of Li-and Mn-rich layered oxide cathode materials. This provides an essential guideline for structural design and stabilization of composite-based cathode materials for lithium-ion batteries.

Conclusions

$Li_{1.2}Mn_{0.4}Co_{0.4}O_2$ and $Li_{1.2}Mn_{0.4-x}Mg_xCo_{0.4}O_2$ (x = 0.00, 0.02, 0.04, and 0.06) cathodes were successfully prepared using a sol–gel method. Mg doping significantly affects the microstructure, crystal structure, and local atomic structure of the prepared cathode materials. The cathodes were composite-based materials, exhibiting different phase separation behaviors of their Li_2MnO_3 and $LiCoO_2$ components. The Li_2MnO_3 and $LiCoO_2$ domain sizes both decreased as the Mg content increased, significantly affecting the electrochemical behaviors of the prepared materials. The level of phase transition occurring during cycling also depends on the Mg content. A $Li_{1.2}Mn_{0.36}Mg_{0.04}Co_{0.4}O_2$ cathode material with a small Li_2MnO_3 domain size and appropriate Mn doping (x = 0.04) provided higher reversible capacity, improved cycling stability, and better rate capability. Mg doping can stabilize the structure of a cathode. This occurs because Mg doping increases Mn–O chemical bonding and reinforces interactions of MnO_6-octahedral slabs, which subsequently leads to improved structural stability by retarding structural transformation and degradation during cycling. This work provides a better understanding about the effects of Mg doping on the structural characteristics and degradation mechanisms during cycling. It provides useful information for designing the structure and enhancing the structural stability of composite-based cathode materials for lithium-ion batteries.

Methods

Sample preparation. $Li_{1.2}Mn_{0.4-x}Mg_xCo_{0.4}O_2$ (x = 0.00, 0.02, 0.04, and 0.06) cathode materials were synthesized using a sol–gel method. $Li(CH_3COO)\cdot 2H_2O$ (Aldrich), $Mn(CH_3COO)_2\cdot 4H_2O$(Aldrich), $Co(CH_3COO)_2\cdot 4H_2O$, and $Mg(CH_3COO)_2\cdot 4H_2O$ (Q RëC™) were used as starting materials. Citric acid was employed as a chelating agent with a molar ratio of metal ions to citric acid of 2:1. First, the required amounts of the raw materials were dissolved in deionized water while citric acid was separately dissolved in deionized water. Then, the aqueous citric acid solution was slowly added into the aqueous precursor solution. After that, the mixed solution was vigorously stirred at 80 °C until a gel formed. This gel was dried at 100 °C for 12 h and then pre-heated at 450 °C for 5 h to remove organic compounds. Finally, the obtained mixture was heated at 800 °C in air for 10 h and naturally cooled to room temperature in a box furnace.

Structural and morphological characterization. The local crystal and atomic structures of the prepared electrodes were examined using X-ray diffraction (XRD) (RIGAKU TTRAX III) and X-ray absorption spectroscopy (XAS) (BL. 2.2, SLRI, Thailand), respectively. The morphological and microstructural characteristics of the prepared materials were studied using transmission electron microscopy (TEM) (FEI, TECNAI G2

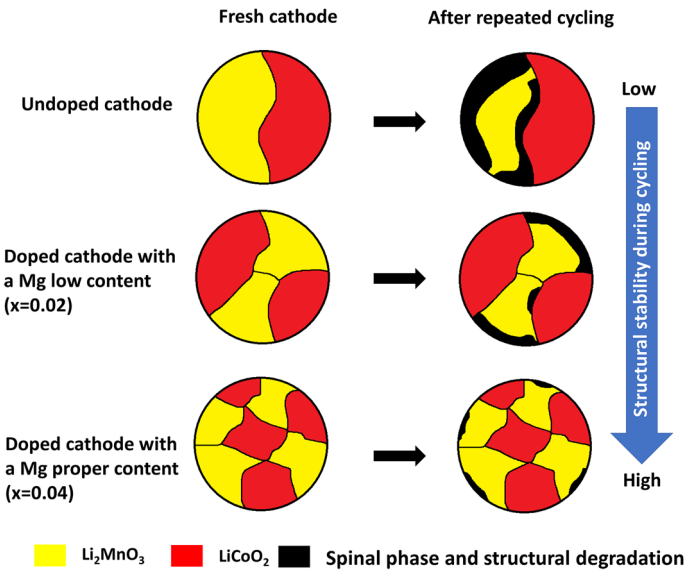

Figure 8. Qualitative illustration of degradation due to structural transition of cathode materials with various Mg dopant levels.

20) and scanning electron microscopy (FEI, Helios Nano Lab G3 C). To estimate the domain sizes of Li_2MnO_3 and $LiCoO_2$, HRTEM images showing clear Li_2MnO_3 and $LiCoO_2$ domains were selected. Then, the selected domains were carefully traced. Afterwards, the areas inside the traced figures were determined using the measuring function of ImageJ software. The 2D areas, obtained from several Li_2MnO_3 and $LiCoO_2$ domains of at least five individual particles with sizes of around 100 nm were averaged. Moreover, X'Pert HighScore Plus software was used to identify the phases of the synthesized materials from the obtained x-ray diffraction patterns. Rietveld refinement was done to calculate lattice parameters. Mn–O, Mn-TM, Co–O, and Co-TM bond lengths were obtained by EXAFS fitting using Artemis software.

Electrochemical characterization. Electrodes were fabricated using a mixture of the synthesized cathode materials, super P carbon black (Alfa Aesar) as a conductive agent, and polyvinylidene fluoride (PVDF, Arkema) as a binder. Synthesized cathode materials, super P carbon black, and polyvinylidene fluoride (PVDF, Arkema) were dissolved in a N-methyl-2-pyrollidone (NMP, Aldrich) solvent at a mass ratio of 80:10:10. Required amounts of these materials were mixed in a shaker for 2 h to obtain a slurry. This slurry was coated onto an aluminum foil using a doctor blade after which it was further dried in a vacuum oven at 80 °C. Haft cells were assembled in an Argon-filled glove box using Swagelok cases. Metallic lithium foil (Alfa Aesar) and 1 M LiPF6 in a 4:3:3 volume ratio of ethylene carbonate (EC): dimethyl carbonate (DMC): diethyl carbonate (DEC) (MTI) were used as the negative electrode and electrolyte, respectively. The separator was made of Celgard 2400. Electrochemical performance including specific capacity, cycling stability, and rate capability of the prepared cathodes was investigated in galvanostatic cycling tests (NEWARE, BTS-4008). Moreover, electrochemical impedance spectroscopy (EIS) (Corrtest, CS310) and a galvanostatic intermittent titration technique (GITT) (NEWARE, BTS-4008) were used to study the electronic conductivity and lithium-ion diffusion coefficients of the prepared electrode materials, respectively.

Data availability

The datasets used and/or analysed during the current study available from the corresponding author on reasonable request.

Received: 29 December 2022; Accepted: 13 March 2023
Published online: 20 March 2023

References

1. Yu, H. & Zhou, H. High-energy cathode materials (Li_2MnO_3–$LiMO_2$) for lithium-ion batteries. *J. Phys. Chem. Lett.* **4**, 1268–1280. https://doi.org/10.1021/jz400032v (2013).
2. Ji, X. *et al.* A review on progress of lithium-rich manganese-based cathodes for lithium ion batteries. *J. Power Sour.* **487**, 229362. https://doi.org/10.1016/j.jpowsour.2020.229362 (2021).
3. Cui, S.-L., Gao, M.-Y., Li, G.-R. & Gao, X.-P. Insights into Li-Rich Mn-based cathode materials with high capacity: From dimension to lattice to atom. *Adv. Energy Mater.* **12**, 2003885. https://doi.org/10.1002/aenm.202003885 (2022).
4. Sathiya, M. *et al.* Origin of voltage decay in high-capacity layered oxide electrodes. *Nat. Mater.* **14**, 230–238. https://doi.org/10.1038/nmat4137 (2015).
5. Choi, A., Lim, J., Kim, H., Doo, S. W. & Lee, K. T. In situ electrochemical Zn^{2+}-doping for Mn-rich layered oxides in Li-ion batteries. *ACS Appl. Energy Mater.* **2**, 3427–3434. https://doi.org/10.1021/acsaem.9b00241 (2019).
6. Xu, B., Fell, C. R., Chi, M. & Meng, Y. S. Identifying surface structural changes in layered Li-excess nickel manganese oxides in high voltage lithium ion batteries: A joint experimental and theoretical study. *Energy Environ. Sci.* **4**, 2223–2233. https://doi.org/10.1039/C1EE01131F (2011).
7. Genevois, C. *et al.* Insight into the atomic structure of cycled lithium-rich layered oxide Li1.20Mn0.54Co0.13Ni0.13O2 using HAADF STEM and electron Nanodiffraction. *J. Phys. Chem. C* **119**, 75–83. https://doi.org/10.1021/jp509388j (2015).
8. He, W. *et al.* Enhanced high-rate capability and cycling stability of Na-stabilized layered Li1.2[Co0.13Ni0.13Mn0.54]O2 cathode material. *J. Mater. Chem. A* **1**, 11397–11403. https://doi.org/10.1039/C3TA12296D (2013).
9. Ates, M. *et al.* Mitigation of layered to spinel conversion of a Li-rich layered metal oxide cathode material for Li-Ion batteries. *J. Electrochem. Soc.* **161**, A290–A301. https://doi.org/10.1149/2.040403jes (2014).
10. Chen, S., Chen, Z., Xia, M., Cao, C. & Luo, Y. Toward alleviating voltage decay by sodium substitution in lithium-rich manganese-based oxide cathodes. *ACS Appl. Energy Mater.* **1**, 4065–4074. https://doi.org/10.1021/acsaem.8b00740 (2018).
11. Li, Q. *et al.* K+-doped Li1.2Mn0.54Co0.13Ni0.13O2: A novel cathode material with an enhanced cycling stability for lithium-ion batteries. *ACS Appl. Mater. Interfaces* **6**, 10330–10341. https://doi.org/10.1021/am5017649 (2014).
12. Jafta, C. J., Ozoemena, K. I., Mathe, M. K. & Roos, W. D. Synthesis, characterisation and electrochemical intercalation kinetics of nanostructured aluminium-doped Li[Li0.2Mn0.54Ni0.13Co0.13]O2 cathode material for lithium ion battery. *Electrochim. Acta* **85**, 411–422. https://doi.org/10.1016/j.electacta.2012.08.074 (2012).
13. Li, Z. *et al.* Stability and rate capability of Al substituted lithium-rich high-manganese content oxide materials for Li-ion batteries. *J. Electrochem. Soc.* **159**, A116–A120. https://doi.org/10.1149/2.044202jes (2011).
14. Knight, J. C., Nandakumar, P., Kan, W. H. & Manthiram, A. Effect of Ru substitution on the first charge–discharge cycle of lithium-rich layered oxides. *J. Mater. Chem. A* **3**, 2006–2011. https://doi.org/10.1039/C4TA05178E (2015).
15. Song, B., Lai, M. O. & Lu, L. Influence of Ru substitution on Li-rich 0.55Li2MnO3·0.45LiNi1/3Co1/3Mn1/3O2 cathode for Li-ion batteries. *Electrochim. Acta* **80**, 187–195. https://doi.org/10.1016/j.electacta.2012.06.118 (2012).
16. Zhao, J. *et al.* Synthesis and electrochemical characterization of Zn-doped Li-rich layered Li[Li0.2Mn054Ni013Co013]O2 cathode material. *Ceramics International* https://doi.org/10.1016/j.ceramint.2015.05.102 (2015).
17. Wei, X. *et al.* Synthesis and properties of mesoporous Zn-doped Li1.2Mn0.54Co0.13Ni0.13O2 as cathode materials by a MOFs-assisted solvothermal method. *RSC Adv.* **7**, 35055–35059. https://doi.org/10.1039/C7RA05106A (2017).
18. Wang, D., Huang, Y., Huo, Z. & Chen, L. Synthesize and electrochemical characterization of Mg-doped Li-rich layered Li[Li0.2Ni0.2Mn0.6]O2 cathode material. *Electrochim. Acta* **107**, 461–466. https://doi.org/10.1016/j.electacta.2013.05.145 (2013).
19. Xu, H., Deng, S. & Chen, G. Improved electrochemical performance of Li1.2Mn0.54Ni0.13Co0.13O2 by Mg doping for lithium ion battery cathode material. *J. Mater. Chem. A* **2**, 15015–15021. https://doi.org/10.1039/C4TA01790K (2014).
20. Nayak, P. K. *et al.* Understanding the influence of Mg doping for the stabilization of capacity and higher discharge voltage of Li- and Mn-rich cathodes for Li-ion batteries. *Phys. Chem. Chem. Phys.* **19**, 6142–6152. https://doi.org/10.1039/C6CP07383B (2017).

21. Jin, Y., Xu, Y., Ren, F. & Ren, P. Mg-doped Li1.133Ni0.2Co0.2Mn0.467O2 in Li site as high-performance cathode material for Li-ion batteries. *Solid State Ionics* **336**, 87–94. https://doi.org/10.1016/j.ssi.2019.03.020 (2019).
22. Li, H. & Fan, L.-Z. Effects of fluorine substitution on the electrochemical performance of layered Li-excess nickel manganese oxides cathode materials for lithium-ion batteries. *Electrochim. Acta* **113**, 407–411. https://doi.org/10.1016/j.electacta.2013.09.135 (2013).
23. Wu, Y. & Manthiram, A. Effect of Al[sup 3+] and F[sup −] Doping on the irreversible oxygen loss from layered Li[Li[sub 0.17] Mn[sub 0.58]Ni[sub 0.25]]O[sub 2] cathodes. *Electrochem. Solid-State Lett.* **10**, 151 (2007).
24. Zhang, H. & Song, T. Synthesis and performance of fluorine substituted Li1.05(Ni0.5Mn0.5)0.95O2−xFx cathode materials modified by surface coating with FePO4. *Electrochim. Acta* **114**, 116–124. https://doi.org/10.1016/j.electacta.2013.10.030 (2013).
25. Park, K. S., Cho, M. H., Jin, S. J., Song, C. H. & Nahm, K. S. The effects of sulfur doping on the performance of O3-Li0.7[Li1/12Ni1/12Mn5/6]O2 powder. *Korean J. Chem. Eng.* **22**, 560–565. https://doi.org/10.1007/BF02706643 (2005).
26. Kang, S. H., Johnson, C., Vaughey, J. T., Amine, K. & Thackeray, M. The effects of acid treatment on the electrochemical properties of 0.5 Li2MnO3·0.5 LiNi0. 44Co0. 25Mn0. 31O2 electrodes in lithium cells. *J. Electrochem. Soc.* **153**, A1186–A1192 (2006).
27. Johnson, C., Li, N., Lefief, C. & Thackeray, M. Anomalous capacity and cycling stability of xLi2MnO3·(1−x)LiMO2 electrodes (M=Mn, Ni, Co) in lithium batteries at 50°C. *Electrochem. Commun.* https://doi.org/10.1016/j.elecom.2006.11.006 (2007).
28. Rossouw, M. H. *et al.* Structural aspects of lithium-manganese-oxide electrodes for rechargeable lithium batteries. *Mater. Res. Bull.* **25**, 173–182. https://doi.org/10.1016/0025-5408(90)90043-2 (1990).
29. Kang, S. H. *et al.* Interpreting the structural and electrochemical complexity of 0.5 Li 2 MnO 3· 0.5 LiMO 2 electrodes for lithium batteries (M= Mn 0.5− x Ni 0.5− x Co 2x, 0≤ x≤ 0.5). *J. Mater. Chem.* https://doi.org/10.1039/b618715c (2007).
30. Kaewmala, S. *et al.* Li2MnO3 domain size and current rate dependence on the electrochemical properties of 0.5Li2MnO3·0.5LiCoO2 cathode material. *Sci. Rep.* **7**, 13196 (2017).
31. Kim, S. *et al.* Synthesis of layered–layered xLi2MnO3·(1–x)LiMO2 (M = Mn, Ni, Co) nanocomposite electrodes materials by mechanochemical process. *J. Power Sour.* **220**, 422–429. https://doi.org/10.1016/j.jpowsour.2012.07.135 (2012).
32. Kaewmala, S. *et al.* Structural and electrochemical kinetic properties of 0.5Li2MnO3·0.5LiCoO2 cathode materials with different Li2MnO3 domain sizes. *Sci. Rep.* **9**, 427. https://doi.org/10.1038/s41598-018-36593-9 (2019).
33. Kaewmala, S. *et al.* A multiscale investigation elucidating the structural complexities and electrochemical properties of layered–layered composite cathode materials synthesized at low temperatures. *Phys. Chem. Chem. Phys.* **22**, 5439–5448. https://doi.org/10.1039/C9CP06165G (2020).
34. Long, B. R. *et al.* Effect of cooling rates on phase separation in 0.5Li2MnO3·0.5LiCoO2 electrode materials for Li-ion batteries. *Chem. Mater.* **26**, 3565–3572 (2014).
35. Croy, J. R., Balasubramanian, M., Kim, D., Kang, S.-H. & Thackeray, M. M. Designing high-capacity, lithium-ion cathodes using X-ray absorption spectroscopy. *Chem. Mater.* **23**, 5415–5424. https://doi.org/10.1021/cm2026703 (2011).
36. Bareño, J. *et al.* Long-range and local structure in the layered oxide Li1.2Co0.4Mn0.4O2. *Chem. Mater.* **23**, 2039–2050. https://doi.org/10.1021/cm200250a (2011).
37. Wang, C. *et al.* Tuning local chemistry of P2 layered-oxide cathode for high energy and long cycles of sodium-ion battery. *Nat. Commun.* **12**, 2256. https://doi.org/10.1038/s41467-021-22523-3 (2021).
38. Thackeray, M. M. *et al.* Li2MnO3-stabilized LiMO2 (M = Mn, Ni, Co) electrodes for lithium-ion batteries. *J. Mater. Chem.* **17**, 3112–3125. https://doi.org/10.1039/B702425H (2007).
39. Xu, H. Y., Wang, Q. Y. & Chen, C. H. Synthesis of Li[Li0.2Ni0.2Mn0.6]O2 by radiated polymer gel method and impact of deficient Li on its structure and electrochemical properties. *J. Solid State Electrochem.* **12**, 1173–1178. https://doi.org/10.1007/s10008-008-0546-y (2008).
40. Grey, C. P., Yoon, W.-S., Reed, J. & Ceder, G. Electrochemical activity of Li in the transition-metal sites of O3 Li[Li[sub (1−2x)/3] Mn[sub (2−x)/3]Ni[sub x]]O[sub 2]. *Electrochem. Solid-State Lett.* **7**, A290. https://doi.org/10.1149/1.1783113 (2004).
41. Kang, K. & Ceder, G. Factors that affect Li mobility in layered lithium transition metal oxides. *Phys. Rev. B* **74**, 094105. https://doi.org/10.1103/PhysRevB.74.094105 (2006).
42. Kaewmala, S. *et al.* Rate dependent structural changes, cycling stability, and Li-ion diffusivity in a layered–layered oxide cathode material after prolonged cycling. *J. Mater. Chem. A* **9**, 14004–14012. https://doi.org/10.1039/D1TA02293H (2021).
43. Ghanty, C., Basu, R. N. & Majumder, S. B. Electrochemical characteristics of xLi2MnO3-(1−x)Li(Mn0.375Ni0.375Co0.25)O2 (0.0 ≤ x ≤ 1.0) composite cathodes: Effect of particle and Li2MnO3 domain size. *Electrochim. Acta* **132**, 472–482. https://doi.org/10.1016/j.electacta.2014.03.174 (2014).
44. Kaewmala, S. *et al.* Rate dependent structural transition and cycling stability of a lithium-rich layered oxide material. *Phys. Chem. Chem. Phys.* **21**, 21984–21990. https://doi.org/10.1039/C9CP04283K (2019).
45. Hong, J., Gwon, H., Jung, S. K., Ku, K. & Kanga, K. Review-lithium-excess layered cathodes for lithium rechargeable batteries. *J. Electrochem. Soc.* **162**, A2447–A2467. https://doi.org/10.1149/2.0071514jes (2015).
46. Bruce, P. G., Robert Armstrong, A. & Gitzendanner, R. L. New intercalation compounds for lithium batteries: Layered LiMnO2. *J. Mater. Chem.* **9**, 193–198. https://doi.org/10.1039/A803938K (1999).
47. Weppner, W. & Huggins, R. A. Determination of the kinetic parameters of mixed-conducting electrodes and application to the system Li3Sb. *J. Electrochem. Soc.* **124**, 1569–1578. https://doi.org/10.1149/1.2133112 (1977).
48. Shaju, K. M., Subba Rao, G. V. & Chowdari, B. V. R. Electrochemical kinetic studies of Li-Ion in O2-structured Li2 / 3 (Ni1 / 3Mn2 / 3) O 2 and Li (2 / 3) + x (Ni1 / 3Mn2 / 3) O 2 by EIS and GITT. *J. Electrochem. Soc.* **150**, A1–A13. https://doi.org/10.1149/1.1521754 (2003).
49. Yu, H. *et al.* Electrochemical kinetics of the 0.5Li2MnO3[middle dot]0.5LiMn0.42Ni0.42Co0.16O2 "composite" layered cathode material for lithium-ion batteries. *RSC Adv.* **2**, 8797–8807. https://doi.org/10.1039/C2RA20772A (2012).
50. Shaju, K. M., Subba Rao, G. V. & Chowdari, B. V. R. EIS and GITT studies on oxide cathodes, O2-Li(2/3)+x(Co0.15Mn0.85)O2 (x=0 and 1/3). *Electrochim. Acta* **48**, 2691–2703. https://doi.org/10.1016/S0013-4686(03)00317-7 (2003).
51. Li, Z. *et al.* Electrochemical kinetics of the Li[Li0.23Co0.3Mn0.47]O2 cathode material studied by GITT and EIS. *J. Phys. Chem. C* **114**, 22751–22757 (2010).
52. Dahbi, M., Urbonaite, S. & Gustafsson, T. Combustion synthesis and electrochemical performance of Li2FeSiO4/C cathode material for lithium-ion batteries. *J. Power Sour.* **205**, 456–462. https://doi.org/10.1016/j.jpowsour.2012.01.079 (2012).

Acknowledgements

This work received a scholarship under the Post-Doctoral Training Program from Khon Kaen University, Thailand [Grant No. PD2565-11] and was partially supported by the Research and Graduate Studies, Khon Kaen University, Thailand. S.K wishes to devote this work to his late and beloved mother (Mooktawee Gaewmala) in appreciation of her endless love and kindness.

Author contributions

N.M., S.K., and P.L. designed this research. S.K., N.K., S.B., P.L., and W.L. carried out the experiments. S.K., N.M., and W.L. analyzed data. N.M., S.S., J.N., and S.K. wrote the manuscript. All authors contributed to the scientific discussion and manuscript revisions.

Competing interests

The authors declare no competing interests.

Additional information

Supplementary Information The online version contains supplementary material available at https://doi.org/10.1038/s41598-023-31492-0.

Correspondence and requests for materials should be addressed to N.M.

Reprints and permissions information is available at www.nature.com/reprints.

Publisher's note Springer Nature remains neutral with regard to jurisdictional claims in published maps and institutional affiliations.